

# Implosion symmetry of laser-irradiated cylindrical targets

R. RAMIS,<sup>1</sup> J. RAMÍREZ,<sup>1</sup> AND G. SCHURTZ<sup>2</sup>

<sup>1</sup>E.T.S.I. Aeronáuticos, Universidad Politécnica de Madrid, Madrid, Spain

<sup>2</sup>CELIA, Université Bordeaux, Bordeaux, France

(RECEIVED 9 July 2007; ACCEPTED 28 February 2008)

## Abstract

We consider the symmetry of cylindrical implosions of laser targets with parameters corresponding to experiments proposed for the LIL laser facility at Bordeaux: eight laser beams in octahedral configuration, delivering a total of 50 kJ of 0.35  $\mu\text{m}$  laser light in 5 ns, impinging on 1.26 mm diameter polystyrene cylindrical shells filled with deuterium at 30 bar and 5.35  $\text{mg cm}^{-3}$ ; this configuration allows to place diagnostics along the symmetry axis to evaluate directly the uniformity of implosion. Numerical studies have been carried out by using the hydrodynamic computer codes MULTI and CHIC, including one-dimensional, and two-dimensional  $R-Z$  and  $R-\theta$  simulations. Deuterium is compressed into a 1 mm long and 50  $\mu\text{m}$  diameter filament, with density ranging from 2 to 6  $\text{g cm}^{-3}$  and temperatures above 1000 eV. In spite of the reduced numbers of beams, a good symmetry can be achieved with a careful choice of the irradiation pattern. The heat transport smoothing between laser absorption zone and ablation layer plays a fundamental role in the attenuation of residual non-uniformities. Also, it has been found that the radiation transport determines the radial structure of the compressed filament.

**Keywords:** Cylindrical targets; Hydrodynamic simulations; Implosion symmetry; Inertial confinement fusion; Laser-plasma interaction

## 1. INTRODUCTION

Experiments with cylindrical targets allow to study the basic physics of the implosion process of inertial fusion capsules driven by either indirect (Hsing & Hofmann, 1997; Hsing *et al.*, 1997) or direct irradiation (Tubbs *et al.*, 1999a, 1999b; Barnes *et al.*, 2002; Lanier *et al.*, 2003; Parker *et al.*, 2004; Fincke *et al.*, 2004, 2005). This sort of open convergent geometry allows, unlike spherical implosions, the observation of the target interior by means of axial diagnostics, and at the same time, it retains important physical phenomena not present in planar experiments, like the Bell-Plesset effect (Bell, 1951; Plesset 1954). In addition, this configuration is relevant for the development of the fast ignition inertial fusion (Tabak *et al.*, 1994; Dunne, 2006), where a compressed mixture of deuterium and tritium has to be ignited by energetic beams, giving place to very complex interaction processes (Honrubia & Meyer-ter-Vehn, 2006; Sakagami *et al.*, 2006; Hora, 2006, 2007; Johzaki *et al.*, 2007). In this context, thermodynamical properties of matter, through the equation of state, play an

important role (Eliezer *et al.*, 2007), and are being studied in different laboratories through experiments with lasers (Batani *et al.*, 2007) as well as with present (Hoffmann *et al.*, 2005), and future (Temporal *et al.*, 2005) heavy ion beams.

The upgrade of the LIL (Ligne d'Intégration Laser) (Kovacs, 2002) to eight beams will take place around 2009. Also, the 3 kJ, 1 ps PETAL laser (Blanchot *et al.*, 2005), now under development, will be available in the same target chamber, and could be used either to generate high resolution diagnostic sources, like proton or fast X-ray radiography, or to interact directly with compressed matter. The first geometrical evaluations of the irradiation pattern to be produced by this laser system (Schurtz, 2004) indicate that cylinders are better adapted to convergent hydrodynamic experiments. Opposite to the experiments done at the OMEGA facility (most of the direct irradiation experiments carried out up to day), we consider a higher energy (50 kJ instead of  $18 \pm 3$  kJ) and a longer pulse ( $>5$  ns instead of 2.5 ns). The laser drive will be active during the whole implosion, up to stagnation; so that low entropy implosions carried out by tailored pulses can be considered. On the other hand, the reduced number of beams (eight instead of 60 at OMEGA) reduces intrinsically the irradiation uniformity

Address correspondence and reprint requests to: R. Ramis, E.T.S.I. Aeronáuticos, P. Cardenal Cisneros 3, 28010 Madrid, Spain. E-mail: rafael.ramis@upm.es

that becomes a critical issue at LIL. We consider here a non-cryogenic target composed of a cylindrical polystyrene shell with 0.06 cm internal radius and 0.003 cm thickness, filled with deuterium at 30 bar and room temperature (density is  $5.35 \text{ mg cm}^{-3}$ ). It must be pointed that mechanical elaboration of such targets with the appropriate degree of symmetry is a technical challenge (Nobile *et al.*, 2006).

Although the density range for fast ignition fusion ( $\approx 400 \text{ g cm}^{-3}$ ) is two orders of magnitude larger than the one possible with these targets, they will allow to study important physical aspects of the scheme, such as the quality and homogeneity of the direct drive implosion and the interaction of a petawatt pulse with a large size core of compressed deuterium. This article is devoted to the characterization of the implosion of such targets, to determine the attainable density, temperature, and size of the compressed core, and to evaluate the timing and symmetry constraints of laser irradiation. Although, in principle, the process is three-dimensional (3D), we can extract useful information from currently available two-dimensional (2D) simulations. We have used the MULTI (Ramis *et al.*, 1988; Ramis & Ramírez, 2004) and CHIC (Abgrall *et al.*, 2004; Weber *et al.*, 2005) codes to study both, the longitudinal and transversal 2D sections of the cylindrical target as well as the 1D averaged problem. A brief description of codes and setting of the numerical model used in this work are given in the Appendix.

## 2. IRRADIATION SCHEME

The arrangement of laser beams on the target is indicated in Figure 1. The eight beams coming in from the vertices of a regular octahedra toward its center, are focused on the cylinder surface (cylinder axis being parallel to one of the edges of the octahedra). Beam center lines intersect cylinder axis with an incidence angle of 54.73 degrees, meeting target surface at points  $F_1 - F_4$  and  $F_5 - F_8$ , located at distance  $Z_f$  of target

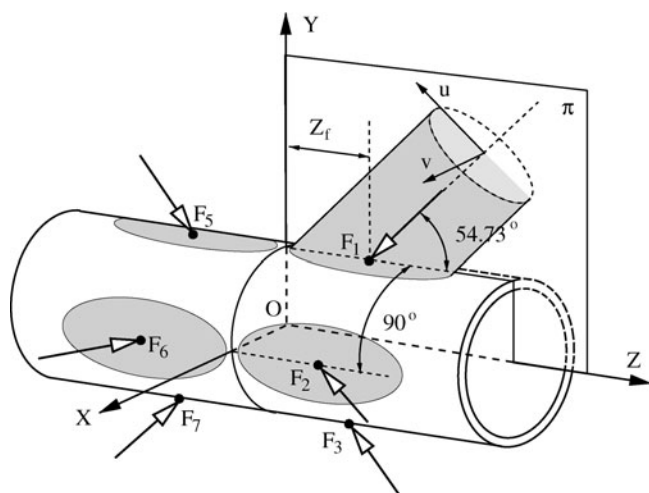


**Fig. 1.** Target irradiation scheme with eight beams in octahedral configuration.

equator. The intensity distribution in the beam cross section is assumed to be in the proximities of the target, super-Gaussian with elliptical shape

$$I \propto \exp\left(-\left(\frac{u^2}{a^2} + \frac{v^2}{b^2}\right)^m\right), \quad (1)$$

where  $u$  and  $v$  are orthogonal coordinates perpendicular to the centerline of the beam, being  $v$  measured in the direction perpendicular to the plane  $\pi$  containing target axis and beam centerline. Typically, we have  $a \geq b$ ; beam section is elongated along the direction of target axis. With these specifications, one can easily compute the irradiation intensity on cylinder surface at initial time. For a cylinder of a given radius  $r$ , the values of  $a$ ,  $b$ ,  $m$ , and  $Z_f$  have been chosen to minimize the root-square-mean (RMS) non-uniformity in the central part of the cylinder surface, defined as the region with length equal to  $r$  (Schurtz, 2004). For  $a = 1.86 r$ ,  $b = 0.93 r$ ,  $m = 2.2$ , and  $Z_f = 0$ , the non-uniformity in the irradiation reaches a 6.08% peak-to-valley and 1.24% RMS. This configuration will be called the *nominal* irradiation pattern through this work. The intensity of irradiation as function of cylindrical coordinates  $Z$  and  $\theta$  is displayed in Figure 2. The isocontours lines are normalized with the average intensity in the central region ( $-1/2 r \leq Z \leq 1/2 r$ ). In the figure, we see clearly the four lobules produced by the pairs of beams focused with  $\theta = \{0^\circ, 90^\circ, 180^\circ, 270^\circ\}$ . The central part pattern is rather complex with eight maxima located at  $Z = 0$  and  $\theta = \{0^\circ, 90^\circ, 180^\circ, 270^\circ\} \pm 29.4^\circ$  and eight saddle points at  $Z = 0$  and  $\theta = \{0^\circ, 45^\circ, 90^\circ, 135^\circ, 180^\circ, 225^\circ, 270^\circ, 315^\circ\}$ . Thick lines correspond to intensity 1, thin continuous lines are spaced 0.1 units, and point lines are spaced 0.01 units. With this scheme, 2.11% of laser beam misses the target and 27.25% of irradiation incises in the  $(1/2 r \leq Z \leq 1/2 r)$  region. Due

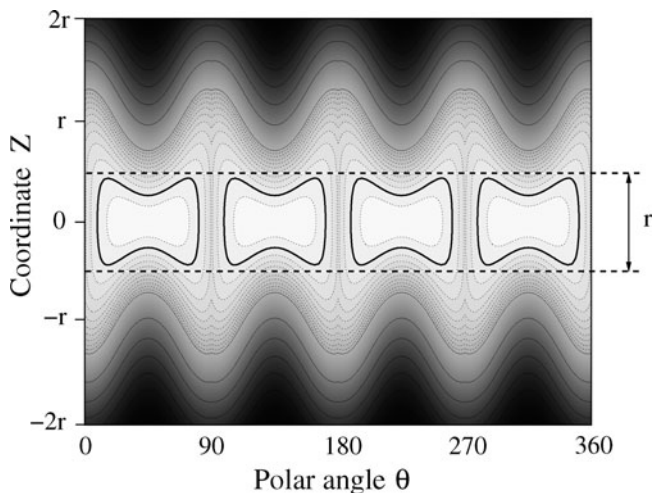


**Fig. 2.** Irradiation pattern on the cylinder surface as a function of cylindrical coordinates  $\theta$  and  $Z$ . The RMS uniformity has been optimized for the region between dashed lines.

to the fact that ablation pressure scales approximately as intensity raised to  $2/3$  (Duderstadt & Moses, 1982; Ramis & Sanmartín, 1983), the initial RMS non-uniformity in pressure and velocity is on the order of 0.75%.

### 3. CYLINDRICAL IMPLOSION

Target evolution is a complex 3D problem. As a plasma corona is generated, laser energy is absorbed volumetrically at densities below the critical one ( $0.0283 \text{ g}\cdot\text{cm}^{-3}$  for fully ionized polystyrene irradiated by  $0.35 \mu\text{m}$  light), and transported from the underdense plasma to the ablation surface mainly by electronic heat conduction. This process generates an ablation pressure that induces the implosion of the central part of the cylinder. As target evolves hydrodynamically, the geometry and absorption pattern are modified. The non-uniformities in the absorption will translate into non-uniformities in pressure and shell position, that will feed back again, giving way to several types of hydrodynamic instabilities. In this context, it is not clear that the rather naive uniformity estimates of previous section is useful to describe properly these targets. Although a full 3D direct simulation is currently not available to us, essential aspects of the problem can be understood by means of 2D studies. First, we will assess the longitudinal uniformity and the extension of the implosion area by means of  $R$ - $Z$  simulations, where laser deposition, computed by 3D-ray tracing, is averaged over azimuthal angles. Laser power (thin line in Fig. 3) is assumed to increase smoothly from zero to 10 TW in  $\tau_r = 1 \text{ ns}$  (power  $\propto \sin^2 \pi t/2\tau_r$ ), to remain constant during 4 ns, and decrease smoothly to zero in 1 ns. The FWHM is 5 ns, and the maximum intensity, evaluated over the initial surface of the target, is  $1.11 \times 10^{14} \text{ W cm}^{-2}$ .

The evolution of the target is summarized in Figure 4. The implosion of the central part takes around 6 ns; a time comparable to the laser pulse. Figures 5 and 6 show snapshots of the *nominal* target at 5 ns, when the equatorial radius has been reduced to one-third; the ablation pressure is around 17 Mbar and the central part of the shell is imploding with a velocity of  $1.65 \times 10^7 \text{ cm s}^{-1}$  and density between 2 and  $6 \text{ g cm}^{-3}$ . The critical density, indicated by the dashed line

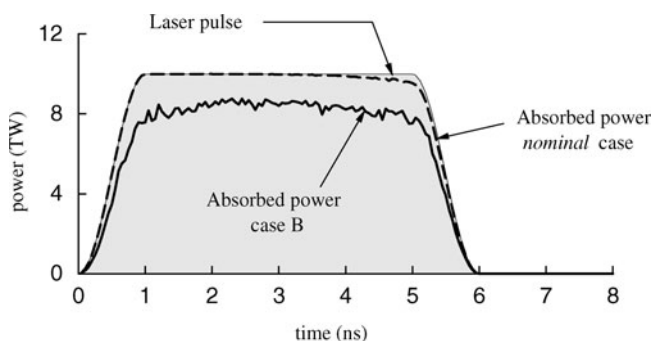


Fig. 3. Laser pulse (thin line) and absorbed energy for the *nominal* and *B* cases.

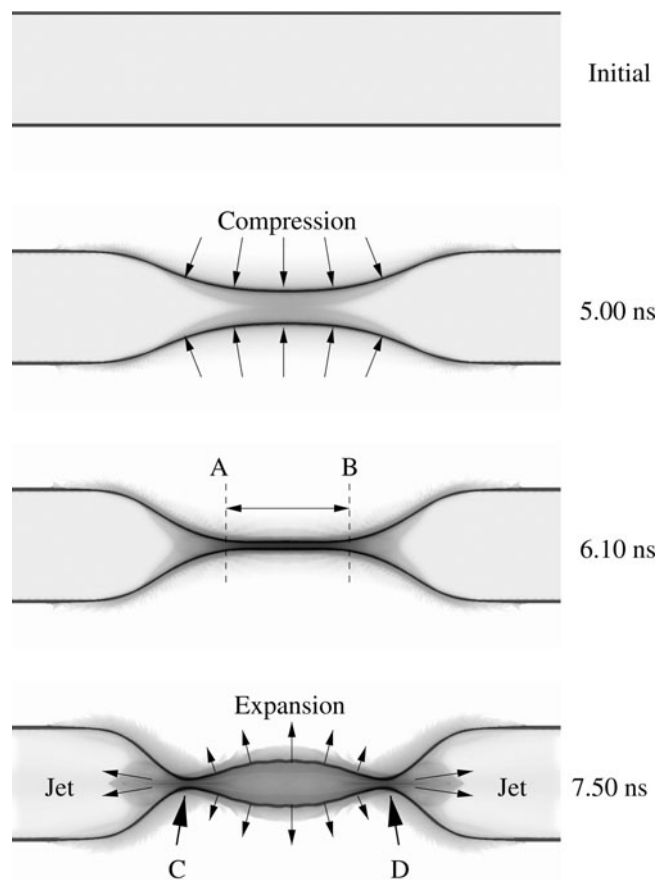


Fig. 4. Time evolution of the *nominal* target.

in Figure 5, is found to be very close to the ablation surface (distance  $\approx 0.0024 \text{ cm}$ ); nevertheless, the critical surface location is not too significant for this problem because most of the laser absorption takes place, mainly by inverse bremsstrahlung, in the external part of the corona.

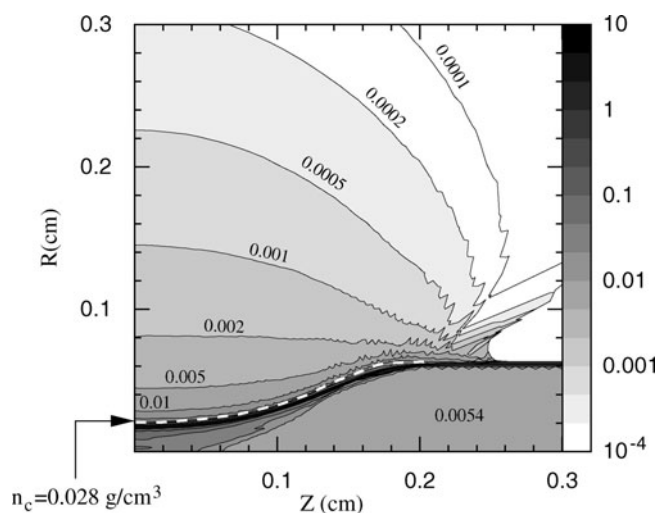


Fig. 5. Density isocontours ( $\text{g cm}^{-3}$ ) for the *nominal* configuration at 5 ns.

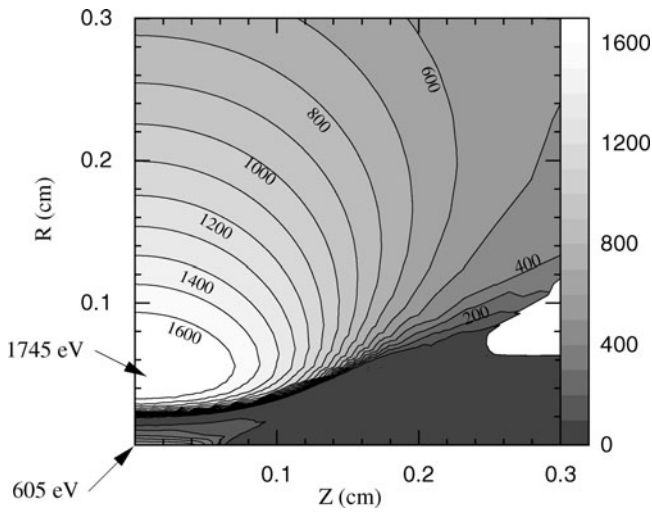


Fig. 6. Temperature isocontours (eV) for the nominal configuration at 5 ns.

At the time of 5 ns, one-half of the power is being deposited at distances larger than 0.048 cm from the axis (more than twice the cylinder diameter at that time) and densities below  $0.005 \text{ g cm}^{-3}$  (one-fourth of the critical). In the corona, temperature reaches a maximum of 1745 eV, inside the region where most of laser energy is deposited.

Figure 3 shows the absorbed laser power as a function of time (thick dashed line). Around 98.7% of the energy is absorbed. This high level, in comparison with experiments (for example, a 70% of energy absorbed for  $10^{14} \text{ W cm}^{-2}$ , 80 ps, and 0.53  $\mu\text{s}$ , (Garban-Labaune et al., 1982)) is due to the larger scale length involved in the present problem. Only at the very beginning of the pulse, when the plasma corona is not yet developed, and at the end of the pulse, when cylinder central part has collapsed to a filamentary form, a small fraction of rays  $\approx 2\text{--}6\%$  misses the target. Limitations in the MULTI code (ray tracing without refraction, complete absorption of the light reaching the critical surface) have been evaluated by simulations with the CHIC code, where all these effects are taken into account. Both codes agree in the very high level of absorption during most parts of the pulse. Differences occur only during the first 2 ns, when the absorption rate computed by CHIC is initially small (as low as 35%) and reaches 80% after 500 ps. At 5 ns, inside the gas filling, the shock wave induced by shell implosion has just converged at cylinder axis, producing a temperature of 605 eV. At later times, after several shock wave rebounds, this temperature will increase to a 1472 eV peak value at 5.85 ns, just before stagnation. The implosion ends by a stagnation phase where a filamentary compressed core (line AB in Fig. 4) is formed. Finally, this core will expand backward, while stagnation is taking place at points (points C and D in Fig. 4) more and more separated from the equatorial plane. In both ends, a complex interaction between shock waves generates axial jets.

Figure 7 shows the deuterium density distribution at stagnation (at time 6.10 ns): internal cylinder radius has been

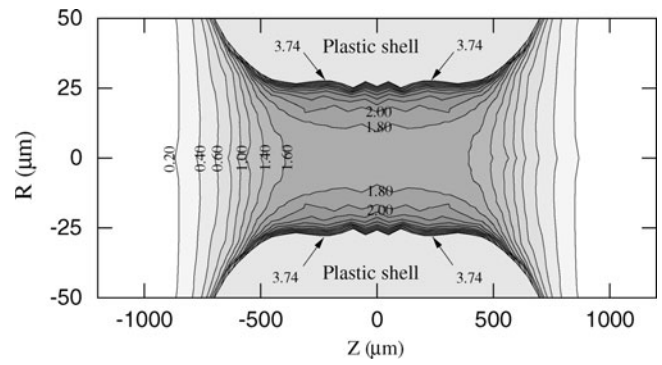


Fig. 7. Density isocontours ( $\text{g cm}^{-3}$ ) for the nominal configuration at 6.10 ns.

reduced to  $27 \mu\text{m}$  (compression ratio of 1:22); central density is around  $1.7 \text{ g cm}^{-3}$ ; and a peak density of  $3.74 \text{ g cm}^{-3}$  occurs at deuterium-polystyrene interface. As density varies radially, the intensity and extension of the implosion should be characterized by the radially averaged density of deuterium

$$\bar{\rho}(z) = \frac{\lambda(z)}{\pi r_i^2(z)}, \tag{2}$$

where  $r_i(z)$  is the radius of the shell interface, and  $\lambda(z)$  is the deuterium axial density

$$\lambda(z) = \int_0^{r_i(z)} \rho(z, r) 2\pi r dr, \tag{3}$$

The  $\bar{\rho}(z)$  profile at stagnation (see Fig. 8) has a peak value of  $2.25 \text{ g cm}^{-3}$  and a FWHM length of 0.1182 cm. The value

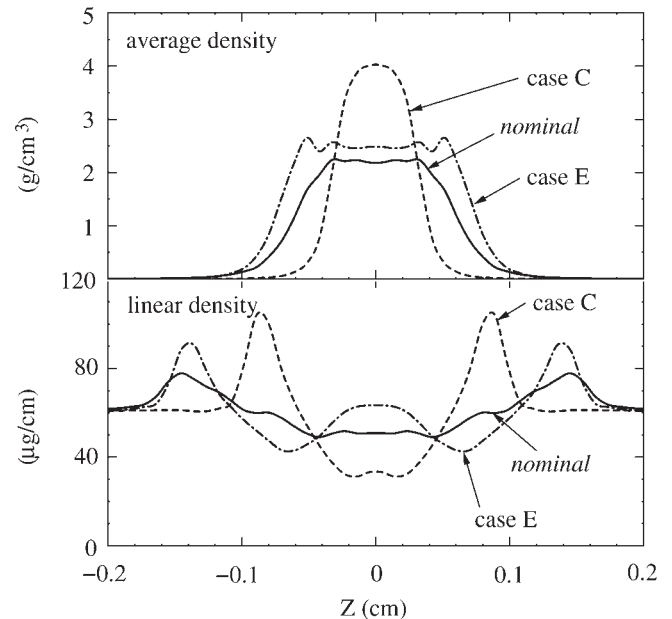


Fig. 8. Radially averaged density  $\bar{\rho}(z)$  and linear density  $\lambda(z)$  for deuterium, at stagnation, for cases: nominal, C and E.

of  $\lambda(z)$  at stagnation is also plotted in Figure 8. At initial time, the cylinder is homogeneously filled with deuterium, so that  $\lambda(z)$  is uniform and equal to  $60 \mu\text{g cm}^{-1}$ . Due to mass conservation, this magnitude would remain uniform in the case of one-dimensional (1D) flow, when the axial component of fluid velocity is zero. For the *nominal* case, there is a 20% reduction of  $\lambda$  in the region where compression takes place; part of the deuterium has been pushed away to the sides, where an increment of  $\lambda$  is clearly visible. At stagnation, the pressure in the central part of the target,  $1700 \pm 100 \text{ Mbar}$ , is essentially uniform. Temperature distribution, shown in Figure 9, reaches a maximum value of 1250 eV and decreases to around 400 eV at the interface between deuterium and polystyrene. In the figure, a thermal wave is visible with temperatures in the range 300–400 eV, ablating the internal side of the polystyrene shell, which main part remains at temperature of 20–40 eV, and density up to  $40 \text{ g cm}^{-3}$ . This structure is discussed in more detail in Section 5. The *nominal* configuration has the inconvenience of requiring elliptical cross section beams ( $a = 0.11718 \text{ cm}$ ,  $b = 0.05859 \text{ cm}$ ). This would obviously complicate the design of the final optics. For this reason, we have also considered the possibility of circular beams ( $a = b$ ) and, in addition, we allow the displacement of beam centerline from target equator (parameter  $Z_f$  defined in Section 2). Table 1 summarizes these alternate designs. Peak  $\rho$  and max  $\bar{\rho}$  are the peak density of deuterium and the maximum of its average density at stagnation,  $t_{stag}$  is the stagnation time, and  $l_{stag}$  is the length (FWHM) of the filamentary compressed region.

Case B, uses circular cross section beams with diameter larger than target diameter. As a consequence, part of the beam misses the target. The corona expansion is not big enough to compensate this fact. Figure 3 shows the absorbed power as a function of time (thick continuous line). Only 81.54% of the energy is coupled to the target, the implosion takes a longer time, and lower densities are reached.

Case C, uses a circular cross section beams with a diameter slightly smaller than the target. The absorption is, as will occur in Cases D and E, almost total. The irradiation is more intense in the equatorial zone, producing a stronger

implosion in terms of implosion time and radially averaged density (see Fig. 8). It must be noticed that due to the smaller size of the compressed core, a large fraction of mass (up to 50%) is pushed out laterally, as can be seen in the same figure.

Case D, uses the same beams as in C, but pointing the center of beam lines to points separated from the equator with  $Z_f = -0.051 \text{ cm}$ . The four beams coming from the right are focussed in the left part of the target, and opposite. The two sets of beams cross each other. The separation distance has been selected in the following way: when  $Z_f$  is zero, case C is reproduced; for large  $|Z_f|$ , two separated implosions occur; for an adequate distance, these two implosions overlap into an uniform one. Results are comparable to the ones for *nominal* case.

Case E is like D, but with positive  $Z_f$  (no beam crossing taking place). The longitudinal motion of mass is complicated as can be seen in Figure 8. The two “separated” implosions push part of the mass to target center. The results are slightly better than in the *nominal* case in terms of achieved density and extension of the implosion.

It is interesting to compare the uniformity of the implosion obtained in the simulations with the theoretical predictions of the simple modeling of Section 2. On the one hand, the numerical uniformity in pressure can be estimated analyzing the displacement of the deuterium-polystyrene interface

$$\xi_{num}(z) = \frac{r_i^o - r_i(z)}{\max |r_i^o - r_i(z)|}, \tag{4}$$

where  $r_i^o$  is the initial radius of the interface. This quantity gives a time integrated measure of the ablation pressure distribution. We choose to evaluate  $r_i(z)$  at the moment when the minimum shell radius is 1/2 of its initial value because earlier times are subject to transient processes with interacting shock waves, and later ones are affected by shell deceleration. On the other hand, from the irradiation pattern  $I(z, \theta)$  defined in Section 2, an averaged value of pressure distribution can be estimated

$$\xi_{theo}(z) = \left( \frac{\int_0^{2\pi} I(z, \theta) d\theta}{\max \int_0^{2\pi} I(z, \theta) d\theta} \right)^{2/3}. \tag{5}$$

In Figure 10, the values of  $\xi_{theo}$  (continuous lines) and  $\xi_{num}$  (dots) are compared for the different cases. For *nominal* and C cases, the agreement is excellent, despite the very simple assumptions in the modeling (static geometry, no lateral transport and transient effects, ...). However, there are some discrepancy in Cases D and E. The cause of this discrepancy is that the theoretical values are computed without taking into account that during shell collapse, Z-coordinate of centerline beam intersection with target surface is continuously changing.

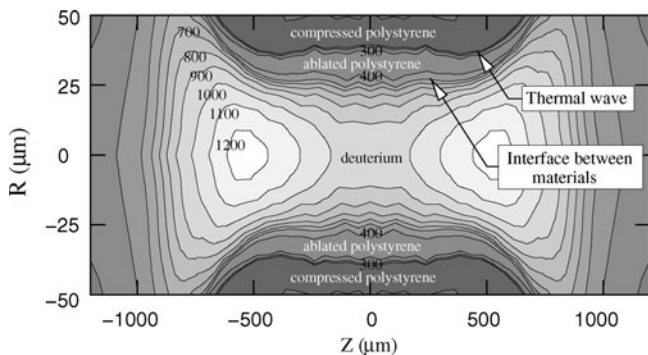


Fig. 9. Temperature isocontours (eV) for the *nominal* configuration at 6.10 ns

**Table 1.** Alternate irradiation schemes

Case	Beam radius (cm)	Offset $Z_f$ (cm)	$t_{stag}$ (ns)	peak $\rho$ ( $\text{g cm}^{-3}$ )	max $\bar{\rho}$ ( $\text{g cm}^{-3}$ )	$l_{stag}$ (cm)
<i>nominal</i>	elliptical, $0.059 \times 0.117$	0	6.10	3.74	2.25	0.1182
B	circular, 0.117	0	7.00	2.83	1.72	0.1318
C	circular, 0.059	0	4.80	4.02	0.0650	
D	circular, 0.059	-0.051	6.05	4.09	2.33	0.1784
E	circular, 0.059	0.063	6.00	4.31	2.66	0.1460

#### 4. AZIMUTHAL UNIFORMITY

In order to evaluate the azimuthal non-uniformity caused by the finite number of beams, a series of  $R$ - $\theta$  simulations of a representative cross section of the target have been performed. Laser cross section is assumed to be super-Gaussian in transversal direction (taking the limit  $a \rightarrow \infty$  in Eq. (1))

$$I \propto \exp\left(-\left(\frac{r^2}{b^2}\right)^m\right) \quad (6)$$

We use  $m = 2.2$  and take  $b$  as a free parameter on the order of magnitude of the initial radius  $r_0$ . Four beams incising with angles  $45^\circ$ ,  $135^\circ$ ,  $225^\circ$ , and  $315^\circ$  are considered. The laser power per unit length has been adjusted by comparing the evolution of the average radius of the shell-gas interface in

the  $R$ - $\theta$  simulation with the equatorial value in the  $R$ - $Z$  simulations of the *nominal* case. A very good agreement is reached by taking  $0.4475 \times 10^{14} \text{ W cm}^{-1}$ , equivalent to an intensity of  $1.13 \times 10^{14} \text{ W cm}^{-2}$  (at initial radius). Figure 11 summarizes the compression performances: the average deuterium density  $\bar{\rho}$  as a function of time for selected values of  $b$ . Figure insets show configurations reached at stagnation.

For extremely small  $b$ , the beams act independently on the cylinder surface producing four localized implosions. For  $b \simeq 0.7 r_0$ , these processes overlap and produce a *cross-shaped* implosion illustrated in Figure 12. From 4.8 ns to 5.2 ns, the shape of the imploding shell changes from a *rhomb* to a *cross*. At that time, the *cross-arms* end their collapse, trapping some of the deuterium filling inside. At 5.6 ns, the central part has already stagnated and some material is

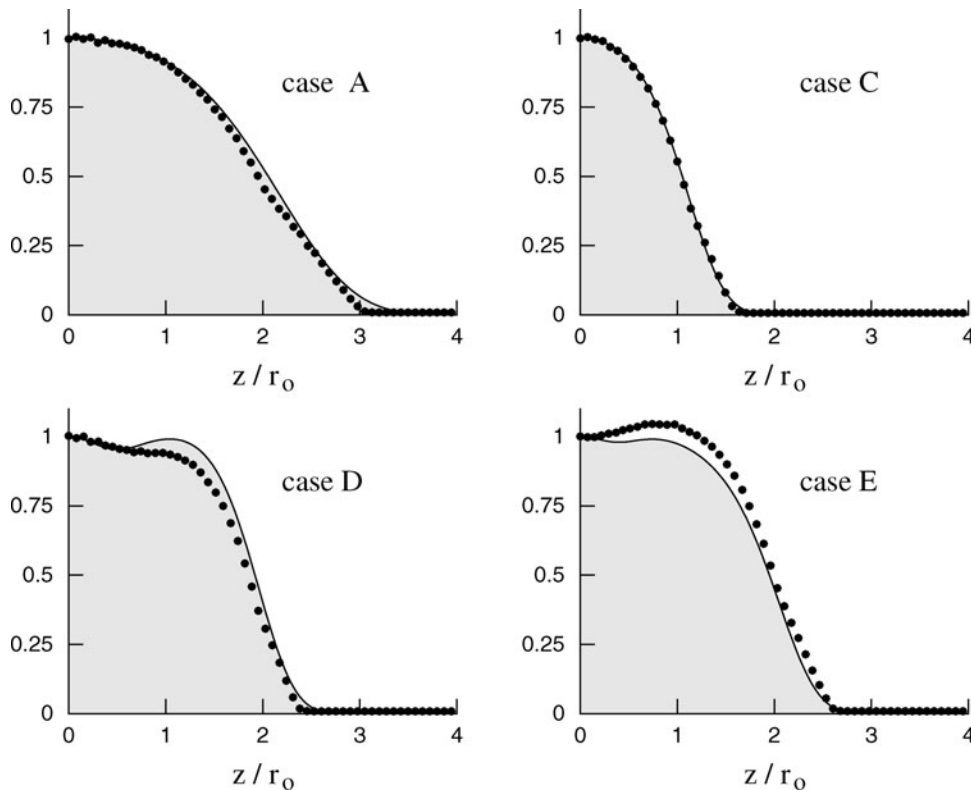


**Fig. 10.** Longitudinal uniformity. Continuous lines ( $\xi_{theo}$ ) are computed theoretically from the specified irradiation pattern, dots ( $\xi_{num}$ ) are obtained from numerical simulations.

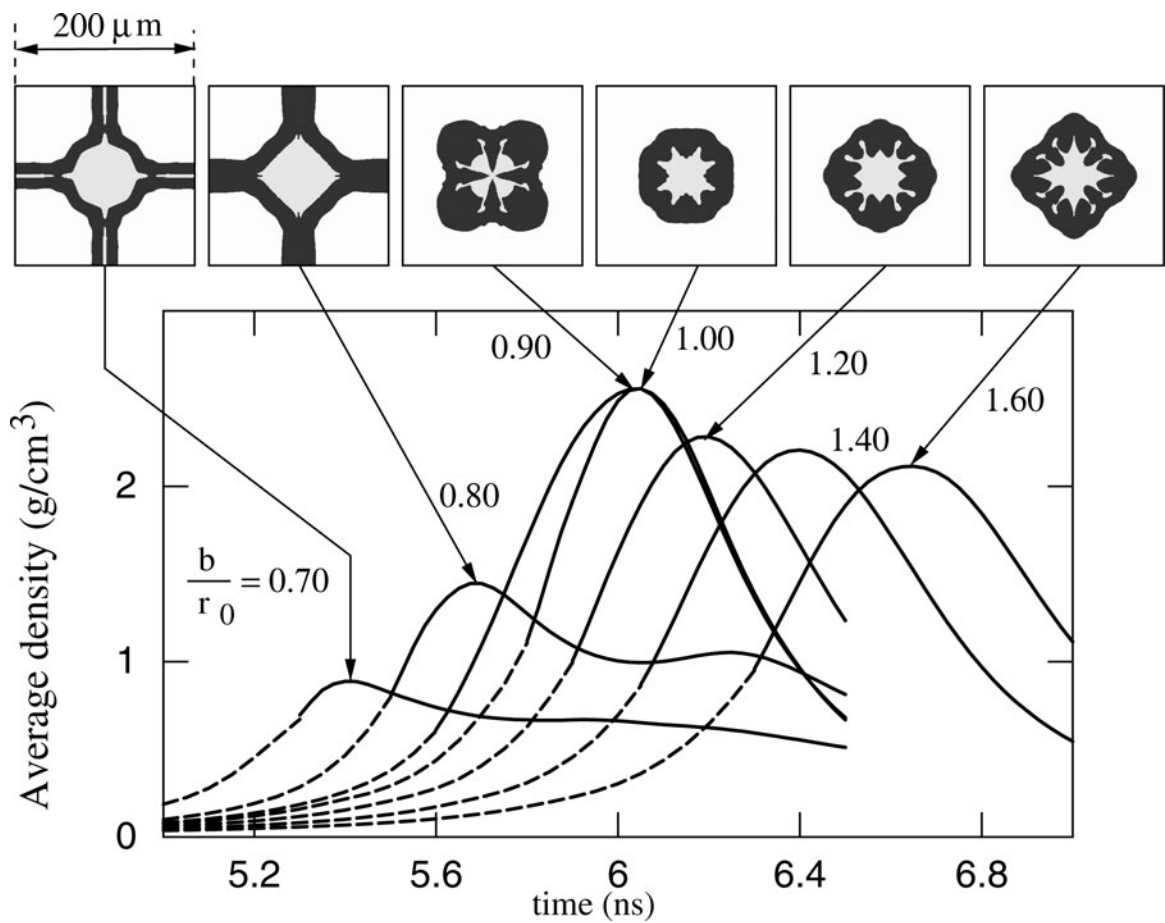


Fig. 11. Average density  $\bar{\rho}(t)$  for  $R-\theta$  cases with different values of  $b/r_0$ . Insets show the compressed core at stagnation. Dashed lines correspond to lagrangian simulations, continuous ones to eulerian simulations.

expanding in  $45^\circ$  direction. *Cross-arms* are exploding laterally and, at the same time, moving to the center. At time 6.0 ns, the target takes the shape of a *flower* with alternate exploding/imploding *petals*. For  $b > 0.7 r_0$ , the structure is

similar but no deuterium is trapped inside the *cross-arms*. Instead, deuterium in the *cross-arms* is pushed out toward target center; for  $b = 0.9 r_0$ , four jets are visible in the corresponding inset of Figure 11.

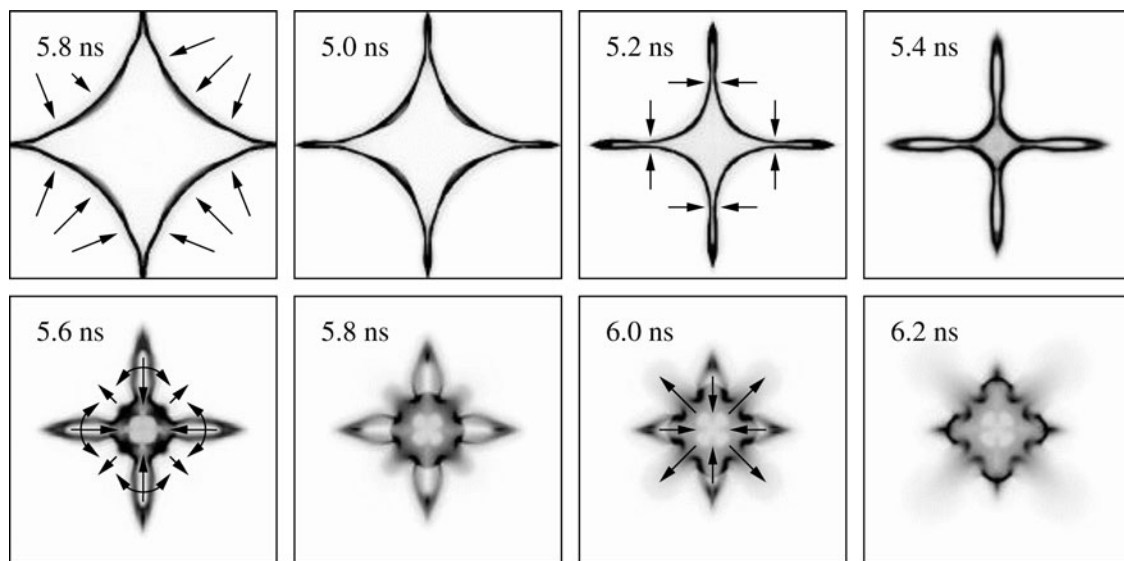


Fig. 12. Cross section of the cylindrical implosion for beam width =  $0.7 \times$  cylinder radius. Squares are of size  $600 \times 600 \mu\text{m}$ .

For  $b \simeq r_0$ , the implosion is more symmetric. Figure 13 shows, for the case  $b = r_0$ , the density and temperature at stagnation. The ripples are due to the non-uniformities in the irradiation, that are transmitted to the internal side of the ablator, and finally amplified during deceleration via Rayleigh-Taylor instability. They have the typical spike-bubble structure on the non-linear phase of this instability. The shape of the deuterium-polystyrene interface is very corrugated, but a central region with a 20  $\mu\text{m}$  radius is composed completely of compressed deuterium, so that we consider this configuration as satisfactory. The attained maximum density 2.5  $\text{g cm}^{-3}$ , peak temperature 1038 eV, and pressure 1.7 Gbar, are quite similar to the ones reached in the *nominal* case on the previous section. In the figure, it is visible a *hot-spot* with different characteristic values of density and temperature for deuterium ( $\simeq 2 \text{ g cm}^{-3}$  and  $\simeq 1000 \text{ eV}$ ) and for polystyrene ( $\simeq 6 \text{ g cm}^{-3}$  and  $\simeq 300 \text{ eV}$ ). This region is surrounded by the cold ablator with higher density ( $\simeq 33 \text{ g cm}^{-3}$ , at spikes) and lower temperature ( $\simeq 30 \text{ eV}$ ). Outside is the plasma corona. At later times, during expansion, the distortion of the interface will increase, giving place to a turbulent mixing between materials.

For large values of  $b$ , the beams are wider than the cylinder, and only the central part interacts with the target. In the limit, this is equivalent to irradiation with uniform unbounded beams. The irradiation pattern takes a simple form, independent of  $b$

$$I(\theta) \propto |\cos(\theta - 45^\circ)| + |\cos(\theta + 45^\circ)|. \tag{7}$$

The RMS non-uniformity is 9.77% in terms of power. The intensity is obviously decreasing inversely proportional with  $b$ , and the average peak density goes as  $b^{-0.6}$ , but the shape of the compressed core does not depend (strongly)

on  $b$ . In Figure. 11, it can be appreciated (for  $b/r_0 = 1.6$ ) that a considerable mixing happens at stagnation.

For moderate  $b/r_0$ , the symmetry of the implosion can be analyzed through the shape of the deuterium-polystyrene interface  $r_i(\theta, t)$ . We can define the numerical asymmetry as

$$\eta_{num}(\theta, t) = \frac{r_i(\theta, t) - r_i^o}{(1/2\pi) \int_0^{2\pi} r_i(\theta, t) d\theta - r_i^o}. \tag{8}$$

This quantity is ideally a measure of the uniformity of the ablation pressure. On the other hand, from the irradiation profile on the target surface one can estimate the theoretical asymmetry as

$$\eta_{theo}(\theta) = \left( \frac{I(\theta)}{(1/2\pi) \int_0^{2\pi} I(\theta) d\theta} \right)^{2/3}. \tag{9}$$

Where  $I(\theta)$  is the irradiation, computed from Eq. (6) on the initial surface of the target. These functions have been plotted in Figure 14 for the case  $b = 1.20r_0$ .

During the first 2 ns, phenomena other than shell acceleration (transient shock waves through the interface) take place, making this quantity non-useful as a measure of the pressure uniformity. From 3 ns to 5 ns,  $\eta_{num}(\theta, t)$  stabilizes to an almost time independent profile. At later time (6 ns), the shell stagnates and again the quantity is non-useful. One can observe that the non-uniformities in the simulation are a factor of 3–4 lower than the values predicted by Eq. (9). The observed reduction is due to the thermal smoothing produced by the diffusive energy transport from the absorption zone to the ablation surface. Let us define  $r_a$  as the radius such that 1/2 of the absorption takes place for  $r > r_a$ . The quotient  $r_a/r_i$  changes with time and takes a value around 1.32 at 3 ns. The fundamental wave number of the azimuthal

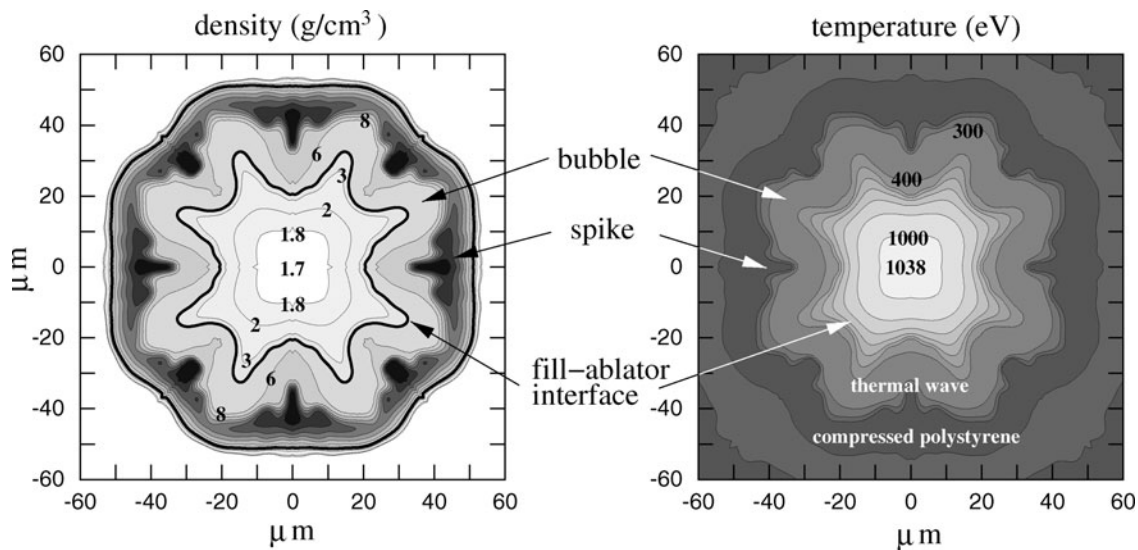
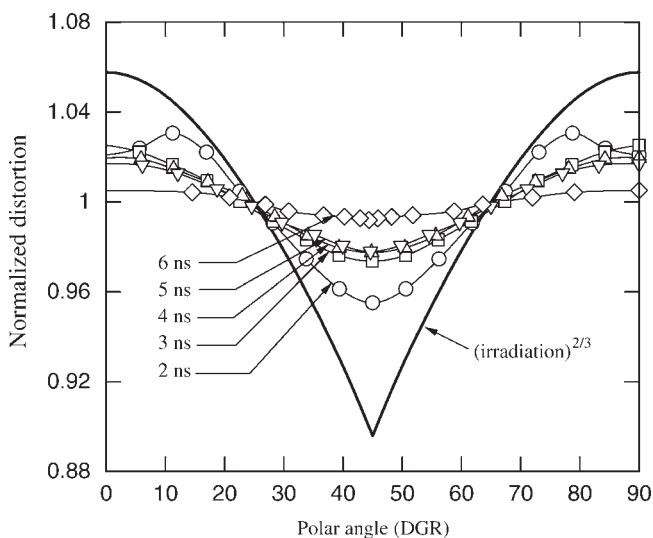


Fig. 13. Isocontours of density and temperature, at stagnation, for beam width = cylinder radius.





**Fig. 14.** Implosion asymmetry for  $b/r_0 = 1.20$ . Thick line ( $\eta_{theo}$ ) is based on irradiation distribution, marks ( $\eta_{num}$ ) correspond to  $R-\theta$  simulations.

perturbations is  $k_\theta \simeq 4/r_i$ . A crude estimate of the damping in radial direction is obtained assuming that energy dumped at radius  $r_a$  is transported to ablation surface at radius  $r_i$ . Neglecting convective terms, the problem is governed by an equation of type  $\nabla^2 T^{7/2} \simeq 0$ . Assuming now quasi-planar geometry, one has  $k_\theta^2 + k_r^2 \simeq 0$ , so that there is a radial damping of the fundamental mode between  $r_a$  and  $r_i$  given by  $\exp(ik_r \Delta r) \simeq \exp(-4(r_a - r_i)/r_i) \simeq 0.3$ . This value is consistent with the smoothing observed in the simulations. This phenomena can be quantified by developing  $\eta_{num}$  and  $\eta_{theo}$  in Fourier series

$$\eta_{num/theo}(\theta) = a_0 + a_4 \cos 4\theta + a_8 \cos 8\theta + a_{12} \cos 12\theta + \dots \quad (10)$$

For  $\eta_{num}(\theta, t)$ , we evaluate the series at  $t = 5$  ns. Figure 15 shows coefficients  $a_4$  and  $a_8$  as functions of parameter  $p \equiv b/r_0$ . The theoretical and numerical curves are similar. The fundamental harmonic  $a_4$  increases with  $p$ , changing sign at  $p = 0.91$  (theory) or  $p = 1.0$  (numerical simulations) (this modest discrepancy is mainly due to the fact that in Eq. (9) a fixed radius is used to compute  $I(\theta)$ ). The second harmonic  $a_8$  is always negative. For  $p > 1$ , one observe a factor of 3 reduction in  $a_4$  and around a factor of 9 in  $a_8$ . For  $p < 1$  things are more complex, but a similar reduction in amplitude would occurs if one *shifts* horizontally the curves to compensate the offset between the theoretical and numerical zeros of  $a_4$ . Finally, for very small values of  $p$ , the distortion is too large to be linearly analyzed.

### 5. COMPRESSED CORE

During the implosion of the target, a series of convergent shock waves are launched into the deuterium gas filling.

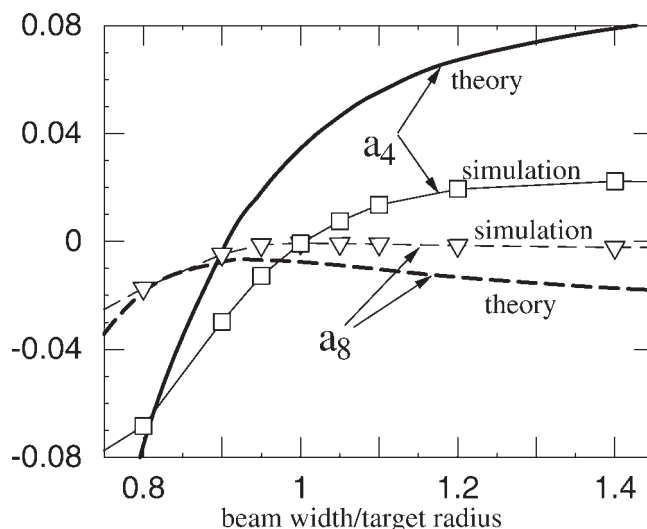


**Fig. 15.** Non-uniformity Fourier coefficient  $a_4$  and  $a_8$  from irradiation distribution model and from  $R-\theta$  simulations.

Multiple shock reflections by the imploding shell take place. The entropy generated in this process induces, at stagnation, the heating of the deuterium gas to temperatures exceeding 1 keV. Energy transport, by electron heat conduction and thermal radiation, smoothes out the hydrodynamic singularities that would occur at target center. Figure 16 shows the radial profiles of density and temperature at stagnation (from 1D simulations, with  $410 \text{ GW cm}^{-1}$ ). One can observe a thermal front (marked TF in the figure) that separates the *hot-spot* central region, with temperatures of several hundred of eV and densities below  $8 \text{ g cm}^{-3}$ , from the cold (10 to 30 eV) and dense shell (up to  $50 \text{ g cm}^{-3}$ ). The thermal front advances into the cold shell ablating material to the *hot-spot*. As indicated in Sections 2 and 3 (see figs 9 and 13), the central *hot-spot* is composed of two different regions: the deuterium filling and the ablated polystyrene, separated by a contact discontinuity (marked DD-CH in the

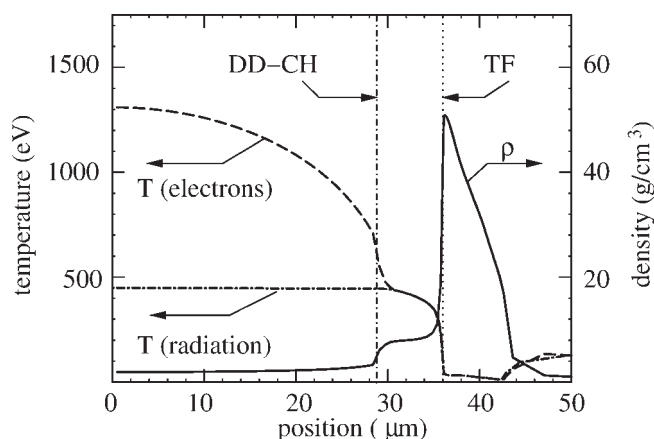


**Fig. 16.** Final compressed configuration with radiative transport enabled. *TF* and *DD-CH* indicate the positions of the *hot-spot* thermal front and the contact discontinuity.

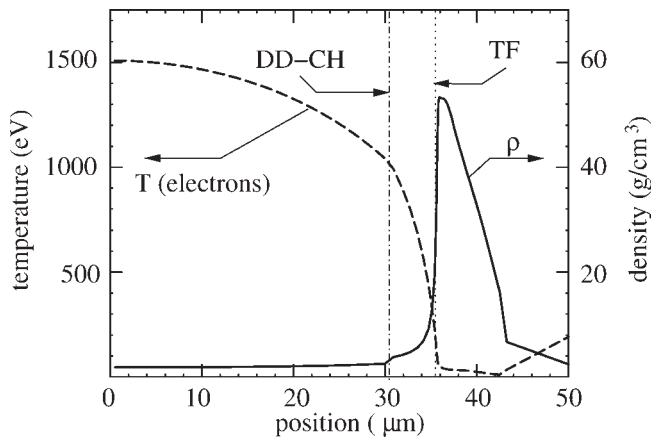


**Fig. 17.** Final compressed configuration without radiative transport. *TF* and *DD-CH* indicate the positions of the *hot-spot* thermal front and the contact discontinuity.

figure). At stagnation, the pressure is essentially the same ( $\approx 2000$  Mbar) in both materials, but temperatures are quite different:  $\approx 1200$  eV and  $\approx 400$  eV, respectively.

The radiation transport role has been investigated here by switching out radiative transport in the simulations (see Fig. 17). Although not crucial, radiation transport modifies the structure of low density plasma blow-off. This has been reported, in the context of its interrelation with nonlocal electronic heat flux (Keskinen & Schmitt, 2007; Schurtz et al.,

2007). Without radiation, due to the absence of radiative losses (7.56% of laser energy), implosion velocity and stagnation pressure are a bit larger:  $18.75 \times 10^6$  cm s<sup>-1</sup> and 2755 Mbar versus  $18.05 \times 10^6$  cm s<sup>-1</sup> and 2445 Mbar. Density and temperature in the dense shell are basically the same. The structure of the *hot-spot* is however quite different; in absence of radiative transport, temperature profile is continuous through both materials, with a change in the slope at the interface, due to different conductivities, and a small jump in density, due to different equations-of-state in the two materials. From these results, we conclude that radiative transport acts in the polystyrene part of the *hot-spot* enhancing the diffusion of thermal energy. The thermal wave goes faster, ablating more material from the shell into the *hot-spot* (from 0.062 mg cm<sup>-1</sup> to 0.122 mg cm<sup>-1</sup>) thus reducing the temperature in this material from 1000 eV to 400 eV. This region is optically thick, and matter is in quasi-equilibrium with thermal radiation. By contrast, the deuterium is optically thin and there is a decoupling between matter temperature and radiation temperature. The radiation temperature in this part (450 eV) is determined by the surrounding optically thick layer.

**6. PULSE SHAPING**

The density attained in the compressed deuterium is determined by the stagnation energy (basically a fixed fraction

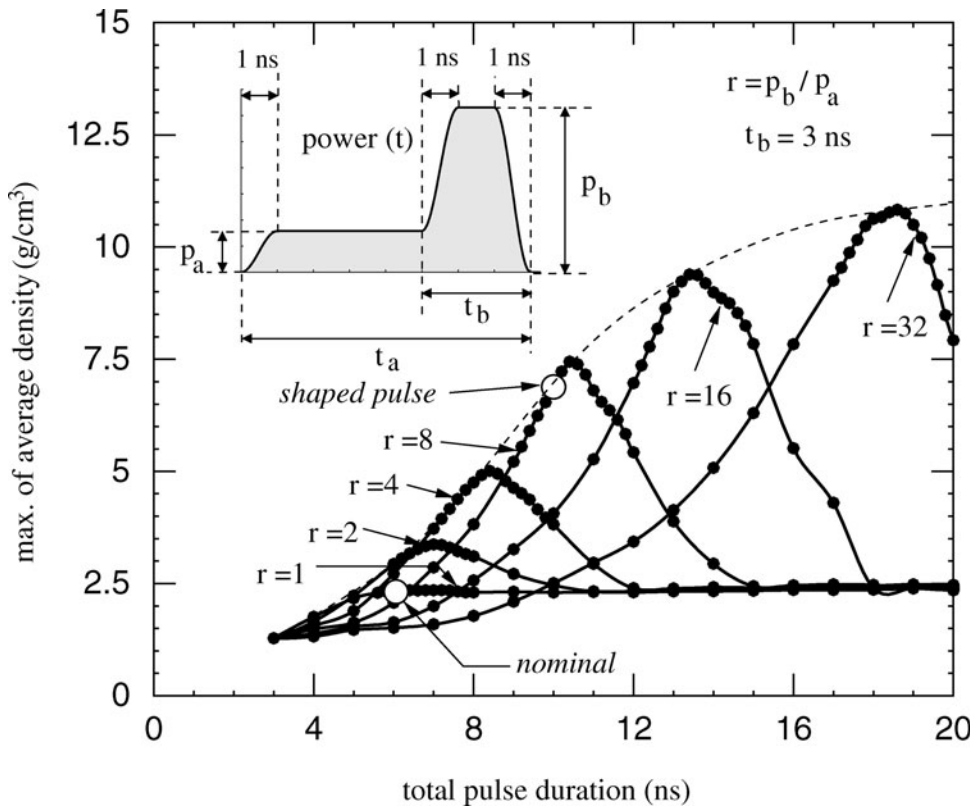


**Fig. 18.** Influence of pulse shape in achieved deuterium compression  $\max \bar{\rho}$ .

**Table 2.** Implosion characteristics

	nominal	pulse shaped
max $\rho$	2.349 g cm <sup>-3</sup>	6.891 g cm <sup>-3</sup>
Stagnation time	5.94 ns	9.89 ns
Stagnation pressure	2445 Mbar	5833 Mbar
Stagnation temperature	1310 eV	1142 eV
Implosion velocity	1.80 × 10 <sup>7</sup> cm s <sup>-1</sup>	1.74 × 10 <sup>7</sup> cm s <sup>-1</sup>
Ablation pressure (prepulse)	–	3.5 Mbar
Ablation pressure (main)	14 Mbar	35 Mbar
Ablated mass	454 μg cm <sup>-1</sup>	462 μg cm <sup>-1</sup>

of the drive energy) and entropy generated during the implosion. The final density can be increased by reducing the entropy by means of a time tailored pulse, composed of a low intensity prepulse, during the shock heating, followed by a main pulse with most of the energy. We consider here pulses with two power levels,  $p_a$  and  $p_b$ , with 1 ns transitions between. Figure 18 shows the results corresponding to a total energy of 2050 J cm<sup>-1</sup>, peak pulse duration  $t_b = 3$  ns, and different values for total pulse time  $t_a$  and power ratio  $r = p_b/p_a$ . The value of  $p_a$  determines basically the implosion time. If the main pulse is launched too early, a strong shock wave heats up the gas to high entropy; if it is launched too late, it misses the compression; so, an optimum must occur for each value of  $r$ . The thin dashed line indicates the maximum compression possible for a given total time  $t_a$ . For other values of  $t_b$ , the results have been found to be similar. We consider the point labeled *shaped pulse* ( $t_a = 10$  ns,  $t_b = 3$  ns,  $r = 8$ ) as a representative high compression design without excessively long laser pulse (the nominal pulse duration of LIL is about 5 ns). Table 2 summarizes the main parameters of the implosions corresponding to the non-shaped and shaped pulses. Several parameters, like implosion velocity, ablated mass, and deuterium temperature at stagnation, depending essentially on the total energy, are quite similar in both cases. Contrarily, the decrease of entropy allows to reach considerably higher densities and pressures in the *pulse shaped* case.

## 7. CONCLUSIONS

The implosion of cylindrical deuterium filled plastic targets to be irradiated by the LIL laser has been analyzed. Deuterium is compressed into a 1 mm long and 50 μm diameter filament, with density ranging from 2 to 6 g cm<sup>-3</sup> and temperatures above 1000 eV (a thermonuclear yield of 10<sup>10</sup>-10<sup>11</sup> neutrons is expected). The longitudinal characteristics of the implosion, extension and uniformity, can be predicted in base to the static analysis of the irradiation pattern. Laser absorption is very high for the considered cases (98.8% for a *nominal* case), while radiative losses are small, around a 7%.  $R$ - $\theta$  simulations show that energy transport, mainly by electronic

heat conduction, between laser absorption zone and ablation surface smoothes out the azimuthal irradiation non-uniformities in a factor of 3–4. This fact allows to reach a relatively homogeneous compressed core using laser beams distributed in only four azimuthal directions and beam radius equal or a bit larger than target radius. It has been found that radiation transport plays an essential role at stagnation phase, determining the final distribution of density and temperature. The laser-pulse can be tailored to improve the attained final density in a factor of 3. Improvements in this direction are constrained by the technically feasible pulse duration.

## ACKNOWLEDGMENTS

The authors would like to express their thanks to J. Breil (CELIA) for many useful discussions. This research has been supported by CICYT of Spain projects FTN 2001-3845, FTN 2003-06901, FTN 2004-01327, ENE 2006-06339/FTN, HF03-186 (Acción Integrada), and by EURATOM/CIEMAT association in the framework of the 'IFE Keep-in-Touch Activities'.

## REFERENCES

- ABGRALL, R., BREIL, J., MAIRE, P.H. & OVADIA, J. (2004). Un Schéma centré pour l'hydro-dynamique Lagrange bidimensionnelle. Report LRC-04-10. Bordeaux, France: Université de Bordeaux 1.
- BARNES, C.W., BATHA, S.H., DUNNE, A.M., MAGELSSSEN, G.R., ROTHMAN, S., DAY, R.D., ELLIOTT, N.E., HAYNES, D.A., HOLMES, R.L., SCOTT, J.M., TUBBS, D.L., YOUNGS, D.L., BOEHLY, T.R. & JAANIMAGI, P. (2002). Observation of mix in a compressible plasma in a convergent cylindrical geometry. *Phys. Plasmas* **9**, 4431–4434.
- BATANI, D., DEZULIAN, R., REDAELLI, R., BENOCCHI, R., STABILE, H., CANOVA, F., DESAI, T., LUCCHINI, G., KROUSKY, E., MASEK, K., PFEIFER, M., SKALA, J., DUDZAK, R., RUS, B., ULLSCHMIED, J., MALKA, V., FAURE, J., KOENIG, M., LIMPOUCH, J., NAZAROV, W., PEPLER, D., NAGAI, K., NORIMATSU, T., & NISHIMURA, H. (2007). Recent experiments on the hydrodynamics of laser-produced plasmas conducted at the PALS laboratory. *Laser Part. Beams* **25**, 127–141.
- BELL, G.I. (1951). Taylor instability on cylinders and spheres in the small amplitude approximation. Technical Report LA-1321. Los Alamos National Laboratory.
- BLANCHOT, N., BIGNON, E., COÏC, H., COTEL, A., COUTURIER, E., DESCHASEAUX, G., FORGET, N., FREYSZ, E., HUGONNOT, E., LE BLANC, C., LOUSTALET, N., LUCE, J., MARRE, G., MIGUS, A., MONTANT, S., MOUSSET, S., NOAILLES, S., NÉAUPORT, J., ROUYER, C., RULLIÈRE, C., SAUTERET, C., VIDEAU, L. & VIVINI, P. (2005). Multi - Petawatt High Energy Laser Project on the LIL Facility in Aquitaine. *Topical Problems of Non-linear Wave Physics* (A. Sergeev, Ed.), *Proc. SPIE* **5975**, 30.
- DUDERSTADT, J.J. & MOSES, G.A. (1982). *Inertial Confinement Fusion*, New York: John Wiley & Sons.
- DUNNE, M. (2006). A high-power laser fusion facility for Europe. *Nature Physics* **2**, 2–5.

- EIDMANN, K. (1994). Radiation transport and atomic physics modelling in high-energy density laser-produced plasmas. *Laser Part. Beams* **12**, 223–244.
- ELIEZER, S., MURAKAMI, M. & MARTINEZ VAL, J.M. (2007). Equation of state and optimum compression in inertial fusion energy. *Laser Part. Beams* **25**, 585–592.
- FINCKE, J.R., LANIER, N.E., BATHA, S.H., HUECKSTAEDT, R.M., MAGELSSSEN, G.R., ROTHMAN, S.D., PARKER, K.W. & HORSFIELD, C.J. (2004). Postponement of saturation of the Richtmyer-Meshkov instability in a convergent geometry. *Phys. Rev. Lett.* **93**, 115003-1-4.
- FINCKE, J.R., LANIER, N.E., BATHA, S.H., HUECKSTAEDT, R.M., MAGELSSSEN, G.R., ROTHMAN, S.D., PARKER, K.W. & HORSFIELD, C.J. (2005). Effect of convergence on growth of the Richtmyer-Meshkov instability. *Laser Part. Beams* **23**, 21–25.
- GARBAN-LABAUNE, C., FABRE, E., MAX, C.E., FABBRO, R., AMIRANOFF, F., VIRMONT, J., WEINFELD, M. & MICHARD, A. (1982). Effect of laser wavelength and pulse duration on laser-light absorption and back reflection. *Phys. Rev. Lett.* **48**, 1018–1021.
- HOFFMANN, D.H.H., BLAZEVIC, A., NI, P., ROSMEJ, O., ROTH, M., TAHIR, N., TAUSCHWITZ, A., UDREA, S., VARENTSOV, D., WEYRICH, K., & MARON, Y. (2005). Present and future perspectives for high energy density physics with intense heavy ion and laser beams. *Laser Part. Beams* **23**, 47–53.
- HONRUBIA, J.J. & MEYER-TER-VEHN, J. (2006). Three-dimensional fast electron transport for ignition-scale inertial fusion capsules. *Nucl. Fusion* **46**, L25–L28.
- HORA, H. (2006). Smoothing and stochastic pulsation at high power laser-plasma interaction. *Laser Part. Beams* **24**, 455–463.
- HORA, H. (2007). New aspects for fusion energy using inertial confinement. *Laser Part. Beams* **25**, 37–45.
- HSING, W.W. & HOFFMAN, N.M. (1997). Measurement of feed-through and instability growth in radiation-driven cylindrical implosions. *Phys. Rev. Lett.* **78**, 3876–3879.
- HSING, W.W., BARNES, C.W., BECK, J.B., HOFFMAN, N.M., GALMICHE, D., RICHARD, A., EDWARDS, J., GRAHAM, P., ROTHMAN, S. & THOMAS, B. (1997). Rayleigh-Taylor instability evolution in ablatively driven cylindrical implosions. *Phys. Plasmas* **4**, 1832–1840.
- JOHZAKI, T., SAKAGAMI, H., NAGATOMO, H. & MIMA, K. (2007). Holistic Simulation for FIREX Project with F<sup>3</sup>. *Laser Part. Beams* **25**, 621–629.
- KESKINEN, M.J. & SCHMITT, A. (2007). Nonlocal electron heat flow in high-Z laser-plasmas with radiation transport. *Laser Part. Beams* **25**, 333–337.
- KOVACS, F. (2002). LIL: status and commissioning. *Proc. Inertial Fusion Sciences and Applications 2001* (Tanaka, K.A., Meyerhofer, D.D. and Meyer-ter-Vehn, J., Eds.) pp. 484–489. Paris: Elsevier.
- LANIER, N.E., BARNES, C.W., BATHA, S. H., DAY, R.D., MAGELSSSEN, G.R., SCOTT, J.M., DUNNE, A.M., PARKER, K.W. & ROTHMAN, S.D. (2003). Multimode seeded Richtmyer-Meshkov mixing in a convergent, compressible, miscible plasma system. *Phys. Plasmas*, **10**, 1816–1821.
- MANHEIMER, W. & COLOMBANT, D. (2007). Effects of viscosity in modeling laser fusion implosions. *Laser Part. Beams* **25**, 541–547.
- NOBILE, A., NIKROO, A., COOK, R.C., COOLEY, J.C., ALEXANDER, D.J., HACKENBERG, R.E., NECKER, C.T., DICKERSON, R.M., KILKENNY, J.L., BERNAT, T.P., CHEN, K.C., XU, H., STEPHENS, R.B., HUANG, H., HAAN, S.W., FORSMAN, A.C., ATHERTON, L.J., LETTS, S.A., BONO, M.J. & WILSON, D.C. (2006). Status of the development of ignition capsules in the US effort to achieve thermonuclear ignition on the national ignition facility. *Laser Part. Beams* **24**, 567–578.
- PARKER, K., HORSFIELD, C.J., ROTHMAN, S.D., BATHA, S.H., BALKEY, M.M., DELAMATER, N.D., FINCKE, J.R., HUECKSTAEDT, R.M., LANIER, N.E. & MAGEISSEN, G.R. (2004). Observation and simulation of plasma mix after reshock in a convergent geometry. *Phys. Plasmas* **11**, 2696–2701.
- PLESSET, M.S. (1954). On the stability of fluid flows with spherical symmetry. *J. Appl. Phys.* **25**, 96–98.
- RAMIS, R. & SANMARTÍN, J.R. (1983). Electron temperature versus laser intensity times wavelength squared: a comparison of theory and experiments. *Nucl. Fusion* **23**, 739–749.
- RAMIS, R., SCHMALTZ, R. & MEYER-TER-VEHN, J. (1988). MULTI - A computer code for one-dimensional multigroup radiation hydrodynamics. *Comp. Phys. Comm.* **49**, 475–505.
- RAMIS, R. & RAMÍREZ, J. (2004). Indirectly driven target design for fast ignition with proton beams. *Nucl. Fusion* **44**, 720–730.
- SAKAGAMI, H., JOHZAKI, T., NAGATOMO, H. & MIMA, K. (2006). Fast ignition integrated interconnecting code project for cone-guided targets. *Laser Part. Beams* **24**, 191–198.
- SCHURTZ, G. (2004). FCI par attaque directe. Utilisation de la LIL en configuration éclatée ou LIL 6 + 2. Report. Talence, France: Université de Bordeaux 1.
- SCHURTZ, G., GARY, S., HULIN, S., CHENAIS-POPOVIC, C., GAUTHIER, J.C., THAIS, F., BREIL, J., DURUT, F., FEUGEAS, J.L., MAIRE, P.H., NICOLAÏ, P., PEYRUSSE, O., REVERDIN, C., SOULLIÉ, G., TIKHONCHUK, V., VILLETTE, B. & FOURMENT, C. (2007). Revisiting Nonlocal Electron-Energy Transport in Inertial-Fusion Conditions. *Phys. Rev. Lett.* **98**, 095002.
- SESAME. (1983). Report on the Los Alamos Equation-of-State Library. T-4 group. Report LALP-83-4. Los Alamos, NM: Los Alamos National Laboratory.
- TABAK, M., HAMMER, J., GLINSKY, M.E., KRUEER, W.L., WILKS, S.C., WOODWORTH, J., CAMPBELL, E.M., PERRY, M.D. & MASON, R.J. (1994). Ignition and gain with ultrapowerful lasers. *Phys. Plasmas* **2**, 1626–1634.
- TEMPORAL, M., LOPEZ-CELA, J.J., PIRIZ, A.R., GRANDJOUAN, N., TAHIR, N.A. & HOFFMANN, D.H.H. (2005). Compression of a cylindrical hydrogen sample driven by an intense co-axial heavy ion beam. *Laser Part. Beams* **23**, 137–142.
- TUBBS, D.L., BARNES, C.W., BECK, J.B., HOFFMAN, N.M., OERTEL, J.A., WATT, R.G., BOEHLY, T., BRADLEY, D. & KNAUER, J. (1999a). Direct-drive cylindrical implosion experiments: simulation and data. *Laser Part. Beams* **17**, 437–449.
- TUBBS, D.L., BARNES, C.W., BECK, J.B., HOFFMAN, N.M., OERTEL, J.A. & WATT, R.G. (1999b). Cylindrical implosion experiments using laser direct drive. *Phys. Plasmas* **6**, 2095–2104.
- WEBER, S., MAIRE, P.H., LOUBERE, R., RIAZUELO, G., MICHEL, P., TIKHONCHUK, V. & OVADIA, J. (2005). A transport simulation code for inertial confinement fusion relevant laser-plasma interaction. *Comp. Phys. Comm.* **168**, 141–158.

## APPENDIX

The code MULTI (Ramis et al., 1988, Ramis & Ramírez, 2004) was developed in a collaboration between the

Universidad Politécnica de Madrid and the Max-Planck-Institut für Quantenoptik in Munich. It integrates the plasma hydrodynamic motion, together with several energy transport mechanisms: electronic heat conduction, thermal radiation, and laser beam deposition. We use here tabulated equations of state from the SESAME library (SESAME, 1983) and opacity tables generated by the SNOP code (Eidmann, 1994). Shock wave capture is allowed by adding, to the thermodynamic pressure, an artificial viscous stress (true physical viscosity plays a secondary role in inertial confinement fusion (Manheimer & Colombant, 2007)). The code is available for either 1D geometry (using separate temperatures for electron and ion species, multigroup radiation transport, and radial laser irradiation) or 2D axial symmetric geometry (one temperature, radiation transport in the gray approximation, and 3D ray tracing without refraction/reflection). For the  $R$ - $Z$  simulations of Section 3, a regular lagrangian grid is used, with 64 intervals in the  $Z$  direction and 16/96 intervals in the  $R$  direction to resolve the deuterium/polystyrene layers (see Fig. 19). The radiation transport is solved by using an angular discretization of the radiation field: the  $4\pi$  direction space is divided into a discrete number of domains (64 in the presented simulations) and an average propagation direction is assigned to each domain. For each direction, the cells are first sorted in the direction of propagation and then the radiation field is obtained by swapping through the grid. For the  $R$ - $\theta$  simulations of Section 4, we approximate the cross section of an infinite cylinder by the section of a torus with a large enough radius (10 cm), two orders of magnitude larger than target diameter. The initial grid is formed by quadrangles. The polystyrene shell is described by a structured grid with 32 intervals per quadrant in azimuthal direction and 96 in radial direction. The central deuterium region is modeled by three curved subregions (A, B and C in Fig. 20) of  $16 \times 16$  cells each, to avoid grid singularity at the origin. The absorption coefficient has been multiplied by  $1/\sin 54.73^\circ = 1.225$  to take into account the laser incidence angle of  $54.73^\circ$ . The  $R$ - $\theta$  simulations are started in lagrangian mode; later, close to stagnation, the grid becomes too distorted, the fluid variables are projected into a new grid, and the simulation is continued in eulerian mode.

For calculations of Sections 5 and 6, where 2D effects are not considered, we use the 1D version of the code. Due to the fact that it uses radially convergent rays, the hydrodynamic efficiency is a bit overestimated: 2445 Mbar (1D) versus 1800 Mbar (2D) peak pressure. On the other hand, this version allows to take into account the partial reflection of laser light at the critical density. It has been found that typically only a  $10^{-6}$  fraction of laser light arrives to the critical surface; numerically, we have total absorption. We have compared the results obtained with several degrees of thermal flux limitation; we consider three values for the flux limiter factor  $f$ :  $10^6$  (no limitation), 0.1 (standard value is this work), and 0.03 (strong inhibition). The results are qualitatively similar in all the cases; by decreasing the value of  $f$  from 0.1 to 0.03,

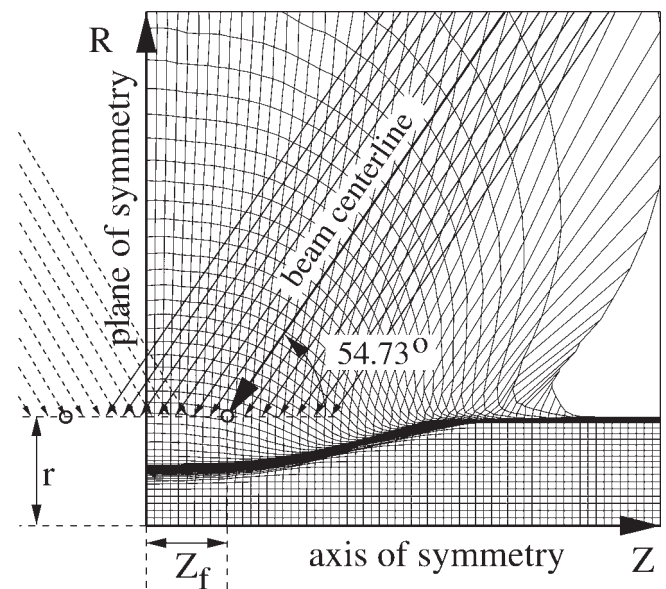


Fig. 19. Typical  $R$ - $Z$  lagrangian simulation.

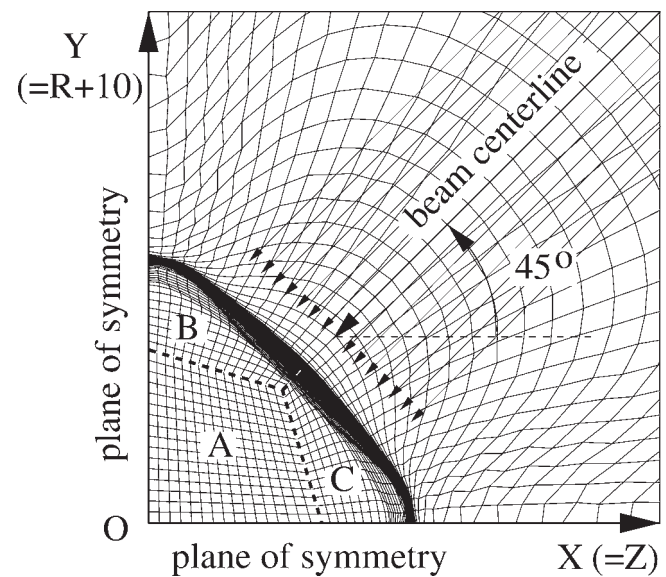


Fig. 20. Typical  $R$ - $\theta$  lagrangian simulation.

temperatures in the corona increases a 20% and the ablated mass decreases a 5%. Smaller variations are found when going from  $f=0.1$  to classical flux. We have also used 1D simulations to evaluate the importance of multigroup transport (not available in 2D). It has been found that some preheating in the polystyrene shell takes place in multigroup simulations; at stagnation, the high density peak in the ablator material is smeared out, being the maximum density reduced from  $50 \text{ g cm}^{-3}$  to  $25 \text{ g cm}^{-3}$ . The structure of the compressed core, discussed in Section 5, is not modified, although the maximum density and pressure decrease about 20%. Also we have seen that the frequency averaged Planck opacity is

more appropriate than the Rosseland one to reproduce multi-group results in this problem.

The CHIC code (Abgrall *et al.*, 2004; Weber, S., *et al.*, 2005) has been developed at CELIA in Bordeaux, for the simulation of laser-plasma interaction processes relevant for applications in inertial confinement fusion. The code consists of a fully nonlinear hydrodynamics in two spatial dimensions using a Lagrangian, discontinuous

Galerkin-type approach, paraxial treatment of the laser field, 3D ray-tracing with refraction and reflection, and spectral treatment of the dominant non-local transport terms. The code uses two matter temperatures (for electrons and ions), realistic equation of state, and electronic heat transport conduction with flux limitation. The code is fully parallelized using MPI in order to be able to simulate macroscopic plasmas.